2018-12-01

An Analytical Model of Material Deformation in Rotary Friction Welding of Thin-Walled Tubes

Caleb James Brown
Brigham Young University

An Analytical Model of Material Deformation in Rotary Friction Welding of Thin-Walled Tubes

Caleb James Brown

A thesis submitted to the faculty of
Brigham Young University
in partial fulfillment of the requirements for the degree of

Master of Science

Tracy W. Nelson, Chair
Carl D. Sorensen
Michael P. Miles

Department of Mechanical Engineering

Brigham Young University

ABSTRACT

An Analytical Model of Material Deformation in Rotary Friction Welding of Thin-Walled Tubes

Caleb James Brown
Department of Mechanical Engineering, BYU
Master of Science

A new model of the material flow in rotary friction welding of tubes is proposed. The material flow proposed is based on 3D scans of welds performed with tungsten tracers. The tracers indicate a bifurcation of flow into two deformation paths. A different analysis is performed on each path.

The material in Path 1 interacts with the weld interface and exhibits large amounts of azimuthal flow. Previous analytical investigations that have analytically modelled the weld interface as a non-Newtonian fluid are used to calculate the strain rate in this zone.

The material in Path 2 transitions from axial to primarily radial flow. The assumption of no azimuthal flow in Path 2 is validated through experimental results of the tracer study. The directional transition in this path is compared to orthogonal machining and equal channel angular pressing. The process to estimate the variables needed to calculate strain and strain rates using the equations from orthogonal machining and equal channel angular pressing is defined.

Strain and strain rate in Path 2 are dependent upon feedrate and upset. Both decrease throughout the welding process. The strain rate is higher than previous studies in rotary friction welding because of the deformation model proposed.

Keywords: Inconel 718, O.T. Midling, O. Grong, material flow, strain, strain rate, model

ACKNOWLEDGEMENTS

This work was funded by GE Global Research. The μCT scans would not have been possible without them, especially Nikole Kucza and Martin Morra. Special thanks to my committee for the insight, advice, and guidance they have provided.

TABLE OF CONTENTS

LIST OF TABLES

LIST OF FIGURES

1 INTRODUCTION

1.1 Introduction to RFW

Rotary friction welding (RFW) is a solid state joining process in which heat is generated by the relative motion at the interface between the work pieces. The heat softens the material, which flows into the flash. This material flow is essential in removing contaminants from the weld interface [1].

There are two types of RFW: inertia friction welding (IFW) and direct drive friction welding (DDFW). In IFW, the rotating piece is attached to a flywheel, whereas in DDFW rotating piece is spun by a motor. In both types of RFW, the system is in a quasi-steady state between the initial torque peak and the braking/forging phase, as shown in Figure 1-1 [1] [2].

Previous studies have concluded that torque, temperature profile, upset rate, flash formation, and deformation patterns all reach a quasi-steady state at the start of the 2nd stage of an RFW [1] [2] [3]. The current paper investigates the material flow during the quasi-steady state stage. The material flow during the quasi-steady state stage in both IFW and DDFW are similar [1].

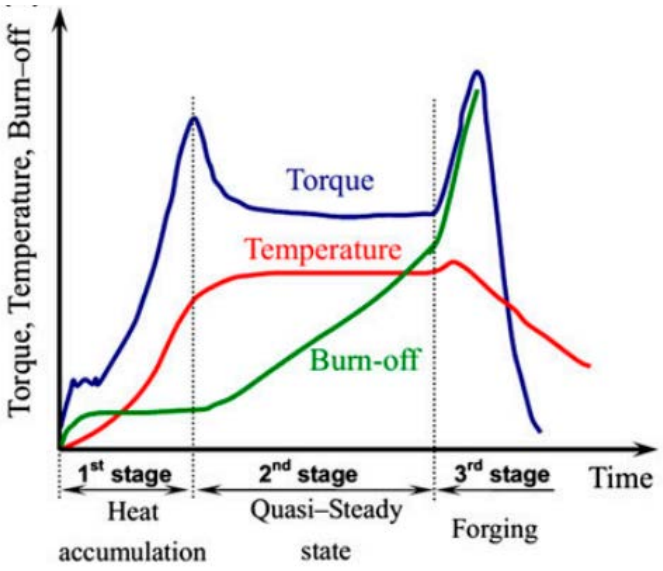

Figure 1-1. Stages of a friction weld [2].

1.2 Coordinate System

A cylindrical coordinate system, as shown in Figure 1-2 is used to describe the direction of material flow [4]. Any flow in the $\bar{\theta}$ direction is assumed to be axisymmetric and is called azimuthal flow.

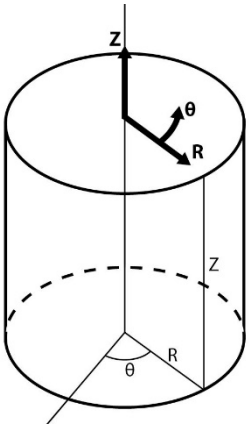

Figure 1-2. Cylindrical coordinates.

1.3 Present Work

The current paper proposes a new model for material flow in the deformation region. The model incorporates the trends found in previous 2D microstructure studies as well as 3D flow patterns investigated in the current paper. The proposed model is the first model to have 3D experimental validation. The deformation patterns found in previous studies and the 3D experiment are used to create a new multi-zone model.

1.4 Previous Models

1.4.1 Four Zoned Model of the HAZ

In literature, the Heat Affected Zone (HAZ) is divided into different zones, as shown in Figure 1-3. As previously defined, the zones are [1] [5]:

- Contact zone (i) – Thin zone where rubbing occurs, inducing large strains and strain rates. Material flow is primarly azimuthal and of large magnitude.
- Fully plasticised zone (ii) – Azimuthal flow is present, but less than the contact zone. Also has large strains and strain rates.
- Partly deformed zone (iii) – Limited azimuthal flow. Significantly lower strains and strain rates when compared to zones i and ii.
- Undeformed zone (iv) – No material flow, but microstructure can be affected by temperature.

These zones are assumed to have a uniform thickness for all values of R [1] [5]. Zones i-iii will refered to collectively as the “deformation region” in the current paper since these are the zones in which material flow occurs.

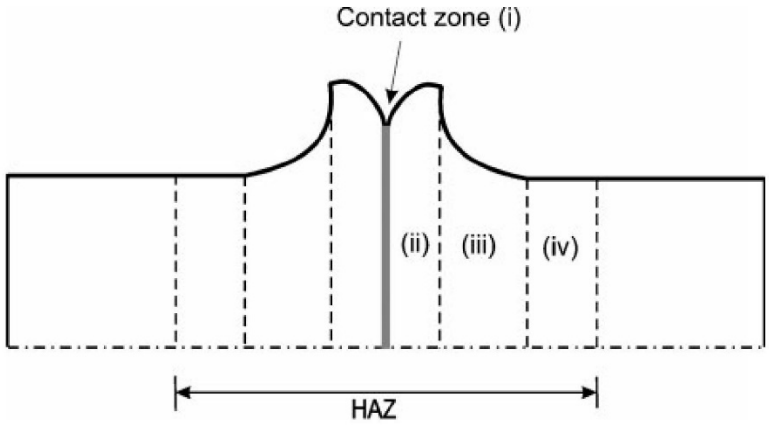

Figure 1-3. Zones within the HAZ [1].

1.4.2 FEA-based Models

Many of the contemporary methods to model material flow during the quasi-steady state stage are FEA-based [3] [6] [7] [8] [9] [10] [11]. The main merit of these methods is the accuracy of the upset, flash profile, and temperature profile [7] [11]. The range of reported strain rates of FEA-based analyses is between 0.5 and 5 [6] [7] [10]. Due to the limitations of remeshing and element size, FEA-based methods cannot capture the high strain rates present at the weld interface [7]. There are several model parameters that affect the calculation of the strain rate including material, mesh size, sample geometry, and heat generation model.

These methods focus on bulk material flow in the deformation region and model the weld interface as a heat generation source. Grant et al. found that the deformation region thickness is non-uniform across the wall thickness, as indicated by the red line in Figure 1-4. Previous studies have used 3D, 2.5D, and 2D FEA models, with none of the models indicating that there is significant azimuthal flow far from the weld interface [6] [10].

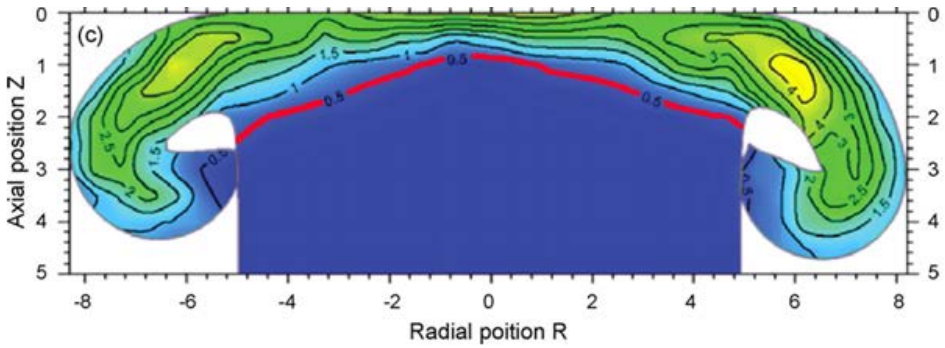

Figure 1-4. Strain rate results of FEA [7].

1.4.3 Analytical Models of Weld Interface

Analytical models have also been created to model the material flow and temperature profile in friction welding [2] [5] [12] [13] [14] [15] [16] [17]. In contrast to FEA-based models, the focus of many of these investigations has been the material flow at the weld interface. The thickness of the deforming material during the heat accumulation stage (1st stage) is significantly smaller than in the other stages, resulting in flow similar to the weld interface during the quasi-steady state stage [12] [13].

In order to analyze the high strain and high strain rate deformation that occurs close to the weld interface, the prevailing assumptions are to model the material as a bingham plastic or highly viscous fluid [12] [13] [15]. These papers report strain rates close to the weld interface between 10^2 and 10^4.

1.4.4 Model Proposed by Midling et al.

Due to the fact that FEA and analytical models capture the material flow at different locations within the deformation region, there is a large difference in the strain rates reported from the two methods. To capture both of the deformation characteristics, Midling et al.

proposed a step-wise 3D velocity field with two regions, as shown in Figure 1-5 [5]. Midling defined the regions as: the fully plasticized region (close to the weld interface) and the partly deformed region (far from the weld interface).

Midling's model makes a distinction between the two regions by specifying different azimuthal flow characteristics. In the fully plasticized region (Z<0.5 in the example from the paper shown in Figure 1-5 and Figure 1-6), there is an azimuthal velocity of large magnitude. The material in the partly deformed region is assumed to have no azimuthal flow. This abrupt change in azimuthal velocity results in the drop in strain rate between the two zones shown in Figure 1-5.

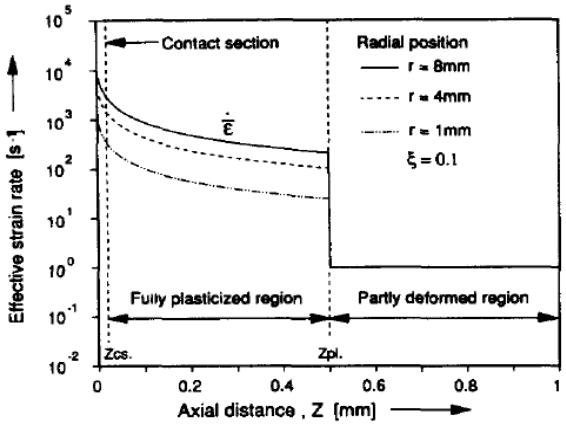

Figure 1-5. Strain rate in deformation region reported by Midling et al.

The strain rate in the partly deformed zone is calculated from the gradient of the velocity field in the RZ plane. The model for the material flow in the RZ plane, for both the fully plasticized region and the partly deformed region, is assumed to rotate about Point A, as shown in Figure 1-6.

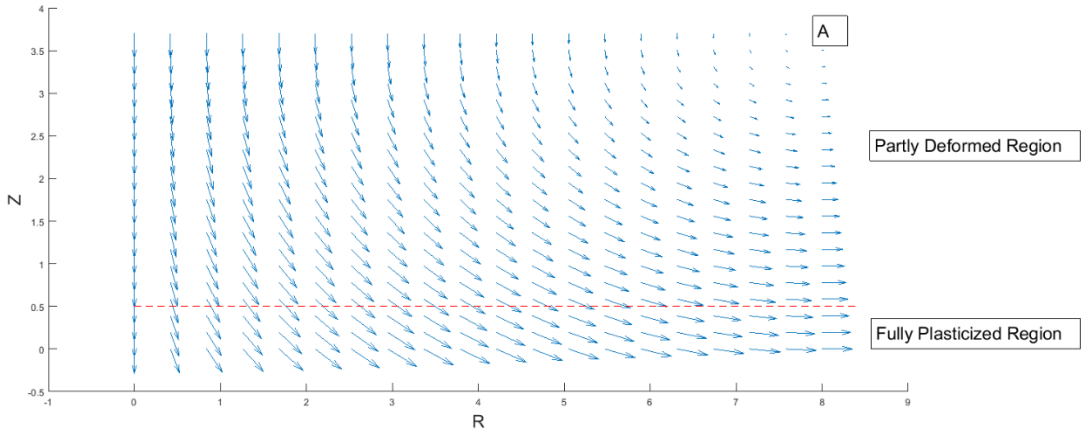

Figure 1-6. Velocity field proposed by Midling et al. in the RZ plane.

When comparing the results from Midling et al. to microstructure analyses, there are discrepancies of how the material transitions from axial velocity to radial velocity. In contrast to Figure 1-6, microstructure analyses indicate that the transition happens abruptly, as illustrated in Figure 1-7 [18]. The material flow indicated by Figure 1-7 can be described by the following pattern:

1) As the material enters the HAZ (as indicated by the blue lines), the microstructure is initially affected by the heat present but there is no change in the direction of flow. The velocity remains axial.
2) The material abruptly transitions velocity as it passes the red line. The location of this transition agrees with the deformation region thickness found by FEA results by Grant et al., as shown in Figure 1-4 [7].
3) The direction of material flow after the turn is radial, as shown by the arrows in Figure 1-7 [18]. The elongated grains behind the parallel parts of the arrows indicate that the flow remains radial until the material is in the flash.

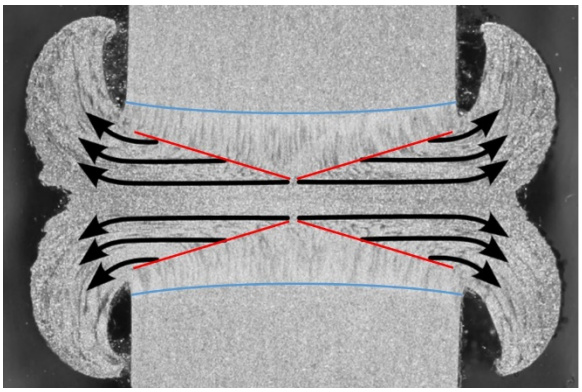

Figure 1-7. Material flow in RFW of steel [18].

Analysis of grain size has calculated the strain at the weld interface using the Zener-Holloman approach to be between $10^{2.4}$ and $10^{2.6}$ [19]. Sketchley et al. studied the microstructure of ODS alloys and found that there was a fine, equiaxed recrystallized zone within 0.5 mm of the weld line, which agrees with the dynamic recrystallization that would occur due to the high strain rates in the fully plasticized zone proposed by Midling [1] [5] [20].

2 METHODS

2.1 Sample Geometry

This paper analyzes the material flow in the RFW of thin walled tubes. The samples have an inside and outside radii of 10.16 and 12.70 mm respectively. A thin wall assumption is made for the current paper. The material is nickel-based superalloy 718. The present study uses DDFW performed at 1000 RPM. The feedrates used in the welds are either 1, 2, or 4 mm/sec.

2.2 Metallography

Metallography was performed using Kalling's No. 2 as an etchant to compare the material flow in the present study to the flow depicted in Figure 1-7.

2.3 Tracer Study

To investigate the material flow, tracers were placed in various locations throughout the wall thickness. A μCT was used to get 3D scans of the welded samples. Tungsten was chosen as the tracer material so that the density of the tracer and sample could be distinguished in the scan. Welds were run with either tungsten wire or tungsten powder as the tracer material. The bulk hot strength of the wire is higher than superalloy 718, which necessitates use of the powdered form as an opposing bound of the material flow of the sample.

2.3.1 Tracer Geometry

The tungsten wire has diameter of 0.229 mm. The powder has an average particle size of 7 microns. Both were inserted into axial holes 0.254 mm in diameter and 2 cm in depth created by a plunge EDM. The location of the center of the hole was measured and the location was non-dimensionalized using the following equation:

$$P = \frac{r_{tracer} - 0.5 * ID}{0.5 * (OD - ID)} - 0.5 \qquad (1)$$

This equation is defined such that the ID, center of the wall thickness, and OD are -0.5, 0, and 0.5 respectively.

2.3.2 Measurement of ϕ

To quantify the material flow in the azimuthal direction, the angle ϕ is measured by the method shown in Figure 2-1a. The green line is drawn through the centers of the undeformed tracer and the tracer in the flash, as shown in Figure 2-1a. Figure 2-1a-c show the same tracer in the Rθ plane at Z values of 1.4, 0.8, and 0.5 mm, respectively, as shown in Figure 2-2. The tracer for all Z values lies on the green measurement line for the angle ϕ, therefore the value of ϕ is assumed constant throughout the entire weld process.

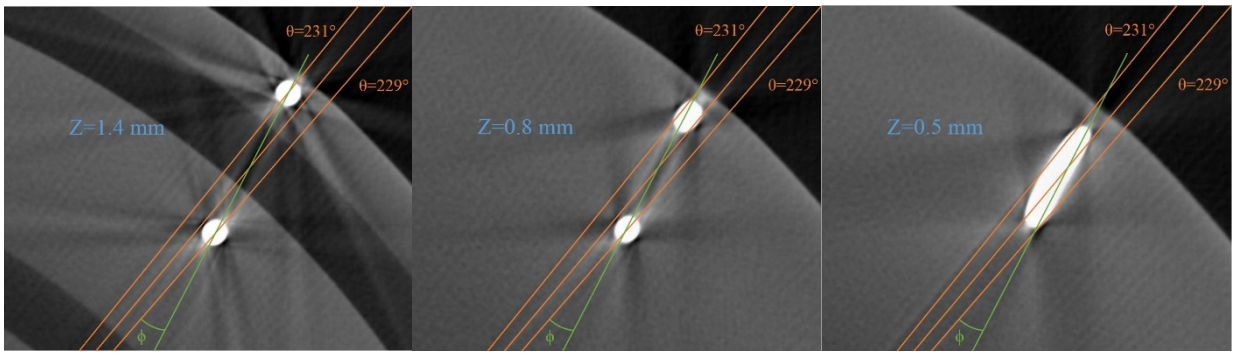

Figure 2-1. Several views of tracer in the Rθ plane and measurement of ϕ.

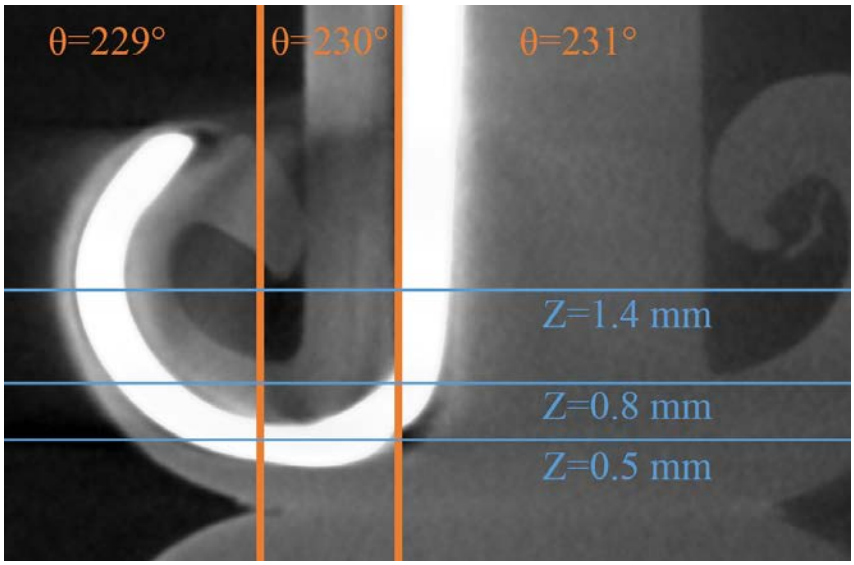

Figure 2-2. Spliced image of tracer in the RZ plane.

2.3.3 Measurement of Tracer Radii

To characterize the material flow in the deformation region, the tracer was viewed in the RZ plane, as shown in Figure 2-2. To quantify the transition from axial to radial material flow, a circle was fit to the tracer within the deformation zone. Each powder tracer exhibited two different radii, with a smaller one closer to the center of the wall thickness, as shown in Figure 2-3. Wire tracers were fit with a single radius. A table with all tracer data, including radii, can be found in Appendix B.

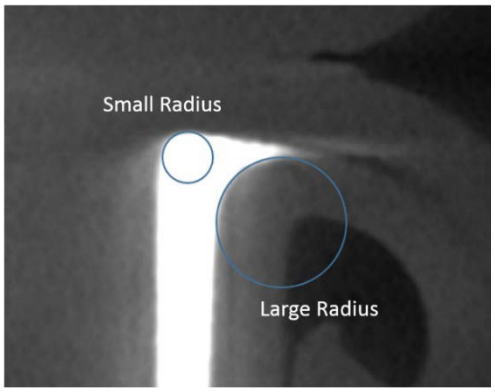

Figure 2-3. Tungsten powder radii.

3 TRACER ANALYSIS

3.1 ϕ Throughout Wall Thickness

The azimuthal displacement of the tracers (ϕ) are plotted as a function of position in Figure 3-1. The data clearly indicates that the amount of azimuthal flow has a strong dependence on position. Material flow close to the center of the wall thickness, -0.1<P<0.1, is primarily azimuthal, ϕ>75°, while material outside of this region exhibits limited azimuthal flow material flow, ϕ<38°. The tracer that does not follow the trend is the result of the wire interacting with both types of material flow simultaneously. A table with all tracer data, including ϕ, can be found in Appendix B.

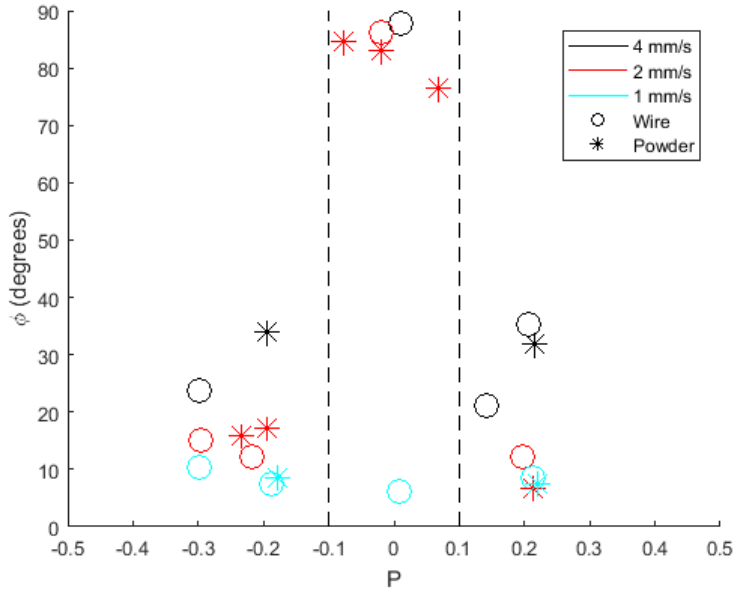

Figure 3-1. Tracer deformation ϕ as a function of position.

The bifurcation of flow into separate zones exhibiting either high or low azimuthal has been assumed in many previous models [1] [5] [7], but this is the first investigation with experimental results to validate the assumption. Previous models have assumed that position within the wall thickness has no effect on the zones, as shown in Figure 1-3. 2D validation, lacking the azimuthal component of material flow, has been available in the past through microstructure studies, but the use of tracers and μCT scans has given new 3D insight into the azimuthal material flow throughout the wall thickness.

3.2 ϕ as a Function of Feedrate

Figure 3-2 shows the dependency of ϕ on feedrate (F). The azimuthal flow of tracers outside the central region (P<-0.1 and P>0.1) show a linear dependency on feedrate over the range of feedrates used in the current study.

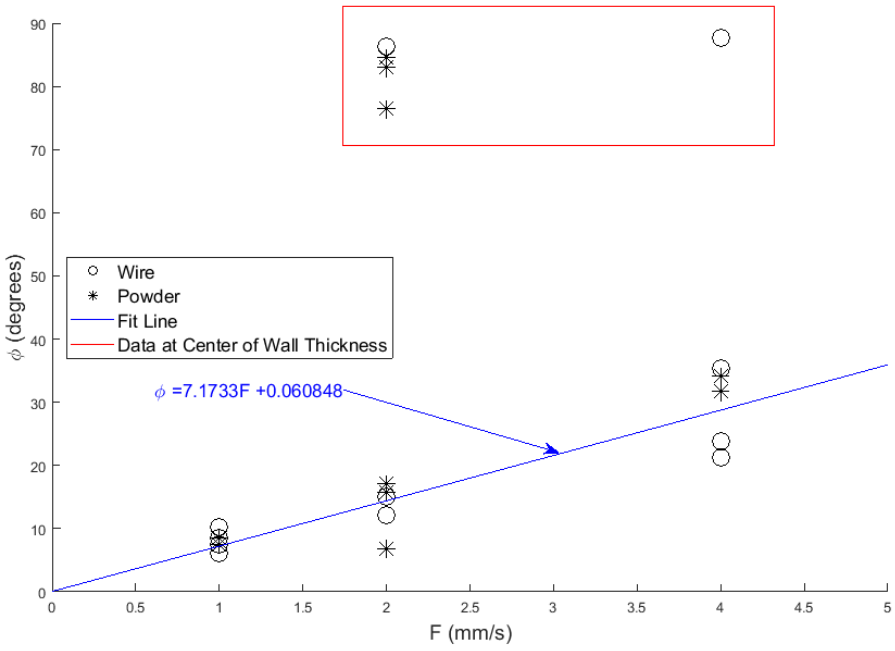

Figure 3-2. ϕ as a function of feedrate.

The increase in ϕ with feedrate is expected given that faster feedrates have higher magnitudes of torque, which would promote larger azimuthal deformation.

3.3 Tracer Radii throughout the Wall Thickness

The tracer study also provides insight into the material flow in the deformation zone through the measurement of the tracer radii. The tracer radii throughout the wall thickness can be used to evaluate the relationship between position and radii proposed by Midling et al. in Figure 1-6. In the model, the material at the center (R=0) exhibits a large deformation radius and the material at the edge of the sample exhibits and infinitesimally small deformation radius, as indicated by the dashed line in Figure 3-3.

The absolute value of P is used as the position variable in order to enable a comparison between the tubular specimens in the current investigation and the solid samples in the study by Midling et al. This allows both position variables to always be positive and measure the distance from the point of symmetry (R=0 in solid and P=0 in tube). The point of symmetry in tubular specimens of P=0 is assumed based on of an analysis of the tracer welds performed with powder tracers placed close to P=0.

3.4 Graphical Comparison to Model Proposed by Midling et al.

The relationship between position and radius as proposed by Midling, as well as the tracer radii from the present study are plotted in Figure 3-3. The y-intercept of the relationship proposed by Midling, indicated by the dashed line, was chosen arbitrarily to show an example of the trend that would be seen if the model proposed by Midling were correct. The relationship

between position and radius proposed by Midling is not supported by the data observed in the current tracer study. A table with all tracer data, including radii and P, can be found in Appendix B.

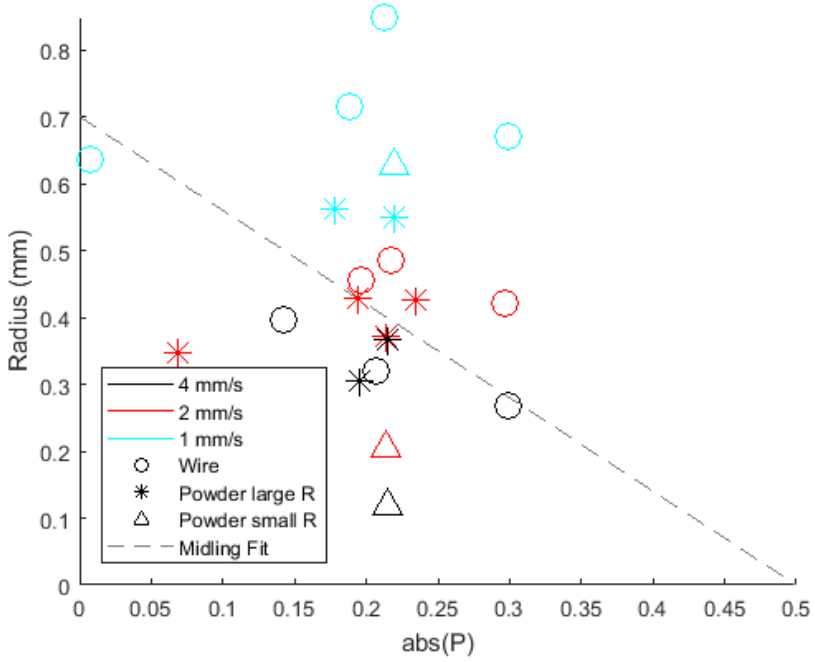

Figure 3-3. Radii of tracers throughout wall thickness.

There are several subsets of data in Figure 3-3 from the tracer study in the present work. These subsets result from different feed rates, tracer material, and powder exhibiting two different radii as shown in Figure 2-3. Some data sets show some dependency on position, as proposed by Midling. The small number of data points in each subset as well as the small range of the position variable both make the analysis of a relationship between position and tracer radii difficult. As such, a simple analysis of Figure 3-3 cannot completely prove or disprove the model proposed by Midling et al. Therefore, a statistical analysis was performed on the data of the

present study in order to quantify the decision to accept or reject the velocity field in the partly deformed region proposed by Midling et al.

3.5 Statistical Comparison to Model Proposed by Midling et al.

3.5.1 Fit Model

To investigate the statistical significance of the position of the tracer on tracer radii, the following equation was fit to the data:

$$R = \frac{C*abs(P)}{F^D} \quad (2)$$

Where C and D are values that are calculated in the fit. This model was chosen because the distribution of the error is normal. In order to be analyzed as a linear equation, a log transform performed on both sides, resulting in:

$$\log(R) = \log(\mathrm{C}) + \log(\mathrm{abs(P)}) - D * \log(F) \quad (3)$$

The values of C and D are group dependent. The grouping variable allows the model to differentiate between wire radii, powder small radii, and powder large radii. This model was chosen because the addition of more variables would increase complexity of the model without increasing the R^2 value. The removal of any term except for log(abs(P)) results in a significant decrease in the R^2 value.

3.5.2 Statistical Results

The only statistically significant variables are feedrate and the tracer type. The position variable abs(P) has a p-value of 0.5526, indicating that the dependency of radius on position as proposed by Midling et al. is statistically insignificant. Therefore, the present analysis disproves

the velocity profile in the RZ plane defined by Midling et al. as a model for material flow in RFW of thin wall tubes.

The statistical significances of allowing C and D to be group dependent are <0.0001 and 0.055, respectively. Therefore, forcing C to be group independent is not statistically advised. Although the dependency of D on the grouping variable is above the normal statistical maximum of 0.05, the p-value of 0.055 is suggestive that D be kept group dependent. Thus, both C and D are defined to be group dependent.

3.6 Fit of Tracer Radii

The equation of the fit of the tracer radii, after removing the position variable from Equation 3, is given as:

$$\log(R) = \begin{Bmatrix} -0.3529 \\ -0.6352 \\ -1.4507 \end{Bmatrix} + \begin{Bmatrix} -0.5724 \\ -0.3676 \\ -0.8364 \end{Bmatrix} * \log(F) \qquad (4)$$

The values within each vector are determined by the tracer radius type. The top, middle, and bottom are the values of the fit for the wire radii, powder large radii, and the powder small radii, respectively. This fit can be used to interpolate between the feedrates used in the current experiment. Extrapolation outside the feedrates used in the current experiment is not validated.

Figure 3-4 shows the results of this fit back transformed into normal axes. By comparing the difference in magnitude between the wire radii and the powder small radii, bounds can be defined of the size of the actual material deformation radii. This model has an R squared value of 0.95.

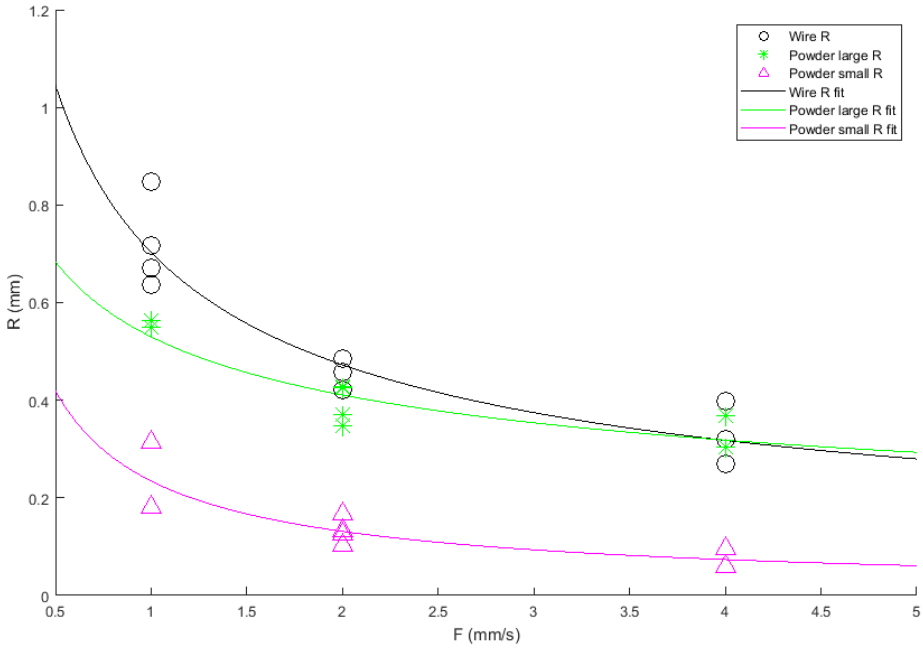

Figure 3-4. Radius as a function of feedrate.

4 PROPOSED MATERIAL FLOW MODEL

The zones and deformation paths in the following proposed model of the material flow were based on the results of the 3D tracer analysis. The model must include a bifurcation of flow where the material near P=0 flows in a primarily azimuthal direction and all other material flows in a primarily radial direction, as indicated by Figure 3-1. As discussed previously, the material flow is assumed symmetric about the P=0. The material not at the middle of the wall thickness undergoes a flow direction transition through a path with a radius that is independent of position, as indicated by the statistical study.

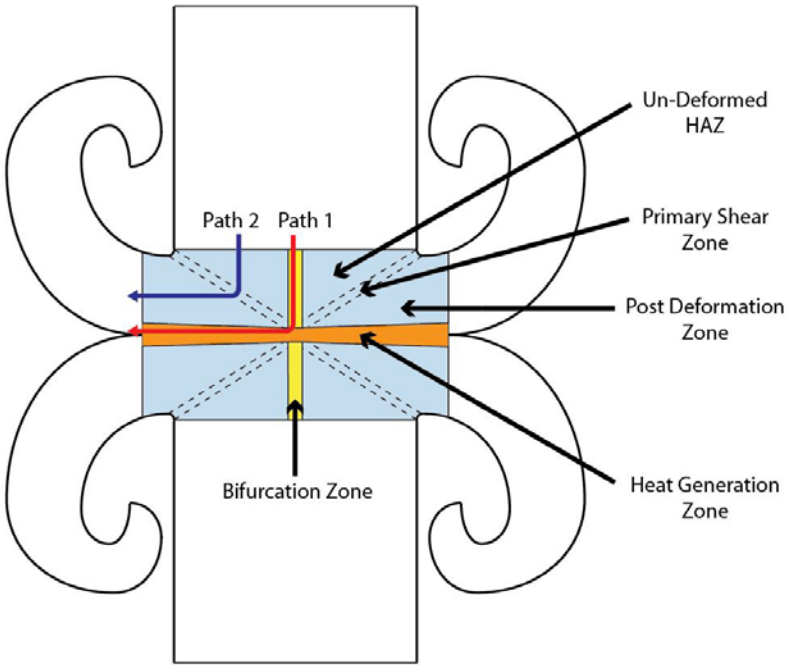

Figure 4-1. Material flow model.

A cross section of the proposed material flow model in the RZ plane is shown in Figure 4-1. As indicated by the bifurcation of flow shown in Figure 3-1, two material flow paths are defined. Path 2 undergoes little azimuthal deformation ($\phi<38°$), whereas Path 1 undergoes significant azimuthal deformation ($\phi>75°$). Path 2 captures the material flow indicated by tracers at P<-0.1 and P>0.1 and Path 1 captures the material flow indicated by tracers at -0.1<P<0.1, of Figure 3-1 and Figure 3-3.

4.1 Description of the Material Flow

Each zone has different material flow characteristics. The description of the material flow in each zone is defined as:

- *Material Flow Path 1*
    - *Bifurcation Zone* – The microstructure in this zone can experience thermal recrystallization. The flow is axial and there is no deformation in this zone. The width of this zone is approximately 0.5 mm (-0.1<P<0.1). The flow is axial and there is no deformation in this zone.
    - *Heat Generation Zone (HGZ)* – This zone includes the weld interface and <0.3 mm of material on each side. Dynamic recrystallization occurs, allowing the material to undergo large values of strain and strain rate. The flow is primarily azimuthal.
- *Material Flow Path 2*
    - *Un-deformed HAZ* – The characteristics of this zone are similar to the Un-deformed HAZ, with the only distinction being the destination of material flow.

- *Primary Shear Zone (PSZ)* – Thermo-mechanically driven recrystallization occurs. In this band, the material transitions from axial to primarily radial flow. The strain and strain rate in this zone are lower than those in Path 1.
- *Post Deformation Zone* – Like the Un-deformed HAZ, there is material flow but no deformation. The increased temperature in this zone affects the microstructure of the material. The material flow in this zone is primarily radial. The amount of azimuthal flow (ϕ) is linearly related to feedrate, as shown in Figure 3-2.

The two paths defined have different material flow characteristics. The bifurcation of material flow necessitates a separate analysis for each path. The following sections will evaluate the strain and strain rates the material undergoes through each path.

5 MATERIAL FLOW PATH 1 ANALYSIS

5.1 Material Flow Description

Path 1 consists of the un-deformed material flow in the Bifurcation Zone and the large azimuthal flow of the HGZ. Material flow in the HGZ is modelled using a previous study of the weld interface [15]. This model does not have a gradient of the azimuthal flow and strain rate, unlike the model by Midling et al. shown in Figure 1-5 [5]. The only difference between the model proposed in this paper and the analysis performed by Francis et al. [15] is the naming of the HGZ.

The HGZ is named for the fact that the majority of the thermal energy needed to increase the material to sufficient temperatures for welding comes from the deformation at the weld interface. This can be deduced from an analysis of total power input in an RFW.

Power input in an RFW must be dissipated within the deformation zone, specifically the PSZ and the HGZ since these are the only zones in which deformation occurs. The power can be split into two terms: the rotational power, which is defined as the torque times the rotational velocity; and the upset power, which is defined as the axial force times the feedrate.

As defined in zone descriptions, the HGZ has no axial flow and the PSZ has little azimuthal flow. Therefore, the rotational power must go into the HGZ and the upset power must go into the PSZ. The magnitude of the rotational power is significantly larger than the upset power. Therefore, the majority of the total power input is through the HGZ.

5.2 HGZ Strain

Given the large azimuthal velocity and small thickness, the strain rate in the HGZ is expected to be large [5]. The equation for the strain rate in the HGZ is [15]:

$$\dot{\gamma}_{HGZ} = \frac{\omega(ID+OD)}{16*B} \quad (5)$$

Where ω is the rotational velocity and B is the HGZ thickness.

The HGZ thickness was measured using tracer studies and metallography. The HGZ thickness is 0.15 mm as measured in welds with powder tracer placed at the center of the wall thickness. The metallography indicated a HGZ thickness of 0.2 mm. These values for the HGZ thickness are smaller than values for the weld interface reported in previous studies in aluminum [5][14]. The discrepancy can be attributed to different sample geometries and material properties. With the HGZ thickness between 0.15 and 0.2 mm, the range in the strain rate calculated using Equation 5 is between $10^{3.5}$ and $10^{3.7}$.

6 MATERIAL FLOW PATH 2 ANALYSIS

Path 2 captures the material flow of the tracers at P<-0.1 and P>0.1. Since the velocity field prosed by Midling et al. is rejected for this path, a new model must be defined. For the model of the material flow in Path 2, this paper utilizes models of other processes that exhibit similar deformation situations. The processes that are used in the comparison are orthogonal machining and equal channel angular pressing (ECAP). Both processes exhibit a 90° turn of the material, which induces a significant amount of shear strain. The equations for strains and strain rates are non-linear and have been investigated in both ECAP [21] [22] and orthogonal machining by previous studies [23] [24] [25].

6.1 Strain undergone in Path 2

This paper uses a thick shear zone analysis of orthogonal machining to model the material flow within the PSZ [23]. This model was chosen for its ability to model the strain and strain rate within the PSZ. The deformation of a unit volume as it passes through the shear zone is from an analysis of the shear strain in ECAP [26]. The model is depicted Figure 6-1.

The angle α is not equal to the complement of λ [22]. α is not be measured in the current investigation given that all strains have been found as a function of λ. The thickness and length of the PSZ, t_{PSZ} and l_{PSZ} respectively, are also shown in Figure 6-1 and are necessary to calculate strain rate.

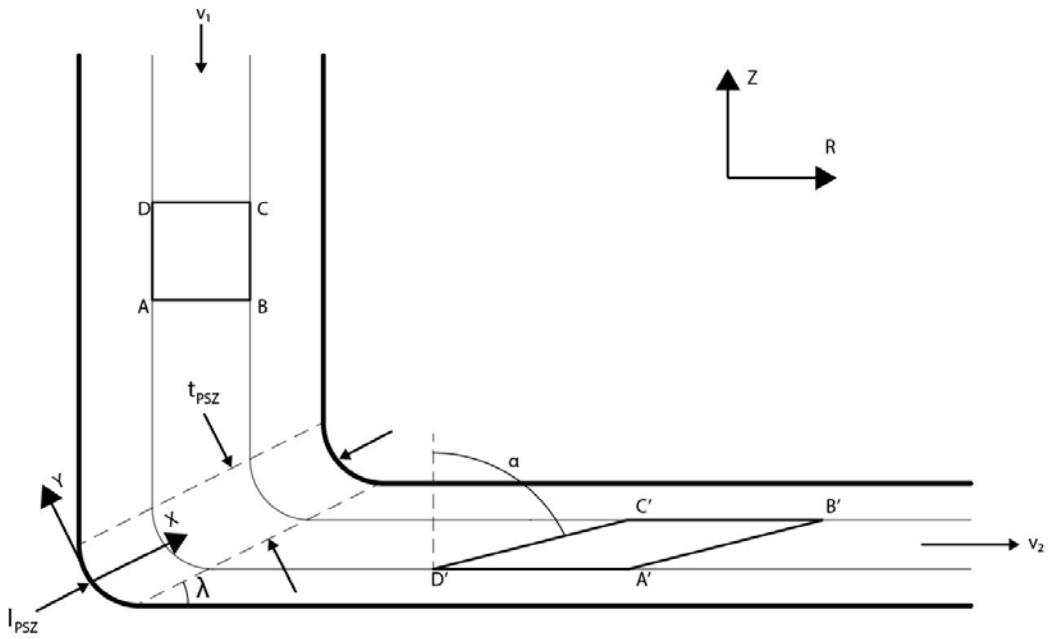

Figure 6-1. Model of the PSZ.

The shear strain in the RZ plane depicted in Figure 6-1 is given in both orthogonal machining [23] [24] [25] and ECAP [21] to be:

$$\gamma_{XY} = \tan(\lambda) + \cot(\lambda) \tag{6}$$

The coordinate frame XYθ is used in this paper to facilitate a comparison of the strain reported in this paper and orthogonal machining.

There is one other shear strain induced upon a unit volume as it passes through the PSZ, which due to the azimuthal flow. This strain cannot be depicted in Figure 6-1. The azimuthal shear in the XYθ coordinate frame is defined as (See Appendix A):

$$\gamma_{X\theta} = \tan(\phi) * \cos(\lambda) \tag{7}$$

$$\gamma_{Y\theta} = -\tan(\phi) * \cos(\lambda + 90°) \tag{8}$$

Previous studies in RFW have not analyzed individual components of strain, but have instead reported an equivalent strain. The individual true strains are combined into an equivalent true strain as [22]:

$$\varepsilon_{eq} = \sqrt{\frac{2\left(\varepsilon_X^2+\varepsilon_Y^2+\varepsilon_\theta^2\right)+\gamma_{XY}^2+\gamma_{X\theta}^2+\gamma_{Y\theta}^2}{3}} \quad (9)$$

The only strains present in the current model are the three shear strains. All axial strains are set equal to 0. The strain rates can also be combined in a similar equation [5].

6.2 Strain Rate throughout Path 2

Figure 6-2 shows the strain rate the material experiences in all locations throughout Path 2 in both the present model (blue line) and the model proposed by Midling et al. (red line). The bell curve of strain rate was defined in previous studies in orthogonal machining [23] [27]. The mean strain rate within the PSZ in the current model is higher than that proposed by Midling et al. This is to be expected given that the transition from axial to radial flow in the model proposed by Midling et al. is smooth, while the current model defines the transition to be an abrupt transition in the PSZ.

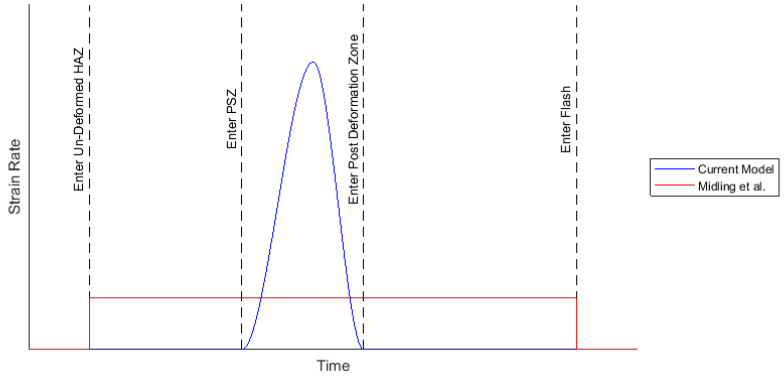

Figure 6-2. Strain rate through Path 2.

The mean value for the strain rate within the PSZ is defined to be half of the peak of the bell curve and is calculated as [23]:

$$\dot{\gamma}_{XY\ Mean} = \frac{F}{t_{PSZ} * \cos(90° - \lambda)} \quad (10)$$

Where F is feedrate and t_{PSZ} is PSZ thickness. Previous studies have not defined equations for $\dot{\gamma}_{X\theta}$ or $\dot{\gamma}_{Y\theta}$ since these strain rates are not present in either ECAP or orthogonal machining.

To calculate the values of $\dot{\gamma}_{X\theta\ Mean}$ and $\dot{\gamma}_{Y\theta\ Mean}$, the results of $\dot{\gamma}_{XY\ Mean}$ (Equation 10) are scaled by the ratio of the respective strains (Equations 7 and 8) and γ_{XY} (Equation 6). The strain rates can be calculated in this manner since it is assumed that the strain rate profiles for $\dot{\gamma}_{X\theta}$ and $\dot{\gamma}_{Y\theta}$ are all similar bell curves to $\dot{\gamma}_{XY}$.

The strains and strain rates discussed in this section are based off theoretical models, with no weld data used in the derivations of the equations. In order to calculate the strains and strain rates for the welds performed in this study, weld data is used.

7 ESTIMATION OF VARIABLES NEEDED FOR STRAIN AND STRAIN RATE IN THE PSZ

The variables needed to calculate the strain and strain rate in Equations 6, 7, 8, and 10 are: F, ϕ, λ, and t_{PSZ}. These variables are estimated for each increment of upset so that strain and strain rate can be plotted as a continuous function throughout the weld process. The methods to calculate these variables are described below.

7.1 Measurement of Feedrate

Feedrate (F) is an input for the weld process and is constant throughout the quasi-steady state stage of the weld.

7.2 Estimation of Azimuthal Flow (ϕ)

The azimuthal flow (ϕ) is necessary when computing $\gamma_{X\theta}$ and $\gamma_{Y\theta}$. Analysis of the tracers in Path 2 (P<-0.1 and P>0.1 in Figure 3-1) show that there is a linear relationship between ϕ and F (Figure 3-2). The parameters of the linear fit are used in the calculation of the strain induced by the azimuthal flow. As discussed with the method of measuring ϕ, the value of ϕ is assumed constant throughout the weld process and equal to ϕ at the end of the weld.

7.3 Estimation of PSZ Angle (λ)

All strains and strain rates are a function of the PSZ angle (λ). This angle determines where the material transitions from axial to radial velocity. The angle λ can be seen in the results of previous FEA and microstructure studies, as shown in Figure 1-4 and Figure 1-7, respectively.

7.3.1 Equation to Calculate λ

At any given increment of upset k, λ can be calculated from the following equation:

$$\lambda_k = \tan^{-1}\left(\frac{t_{FT,k}}{0.25*(OD-ID)}\right) \quad (11)$$

Where $t_{FT,k}$ is instantaneous flash thickness at the increment of upset k. As shown in this equation, the flash thickness at each increment of upset in order to estimate λ throughout the weld process.

A simple linear correlation between flash thickness measurement location and weld upset cannot be made since λ, and therefore exit velocity, is non-constant throughout the weld process. The process to correlate a flash thickness measurement to the correct increment of upset is described in the following paragraphs.

7.3.2 Measurement of Flash Thickness

$t_{FT,k}$ is measured using an image of the welded sample, as shown in Figure 7-1. At each increment of upset, the flash thickness is assumed equal in all four quadrants of the deformation zone. Therefore, the flash thickness measurements in each quadrant, shown in Figure 7-1, are averaged. t_{FT} is measured perpendicular to the red line.

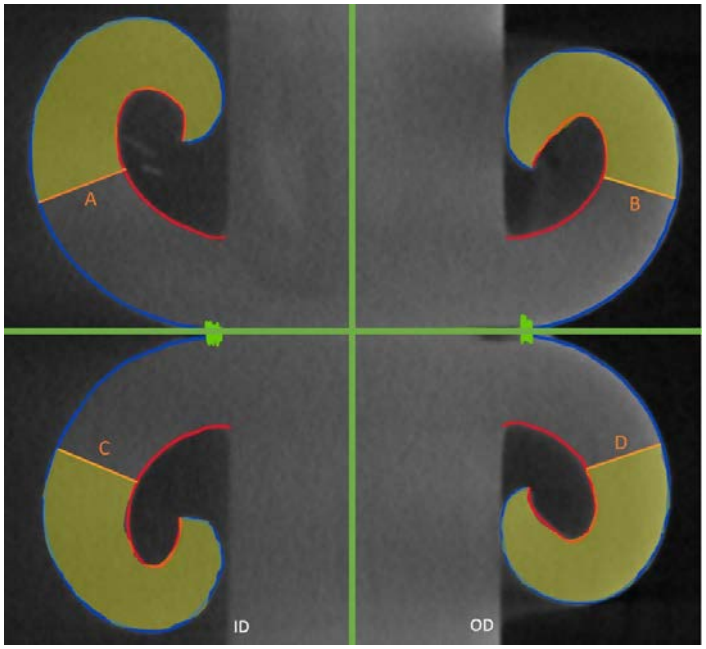

Figure 7-1. Flash thickness measurements.

The four lines should measure the flash extruded from the Post Deformation Zone at the same time step, k. To ensure this, the placement of the lines must be calculated.

7.3.3 Placement of the Lines

Line A is placed arbitrarily, and lines B-D are placed in locations calculated utilizing the volumes of material extruded before each line. The volume of a section of the flash extruded before a given line is calculated using the shell method. This calculation is given as:

$$V_{flash} = 2\pi \iint R \, dRdZ \tag{12}$$

Where R is measured from the center of the sample (not the center of the wall thickness). The area of the flash over which this calculation is performed is indicated by the shaded regions in Figure 7-1.

This calculation is performed on each of the four sections of the flash individually, resulting in individual volumes for each quadrant. The values of the volume calculation V_A, V_B, V_C, and V_D are calculated for lines A-D respectively.

Since line A is chosen arbitrarily, V_A is used as the common comparison when placing the other lines. Line C is placed such that V_C equals V_A, because of the symmetry across the weld interface. Since the Bifurcation Zone assumed to be at P=0 and the specimens are tubes, more material is extruded into the outside flash than the inside flash, as indicated by Equation 13.

$$\frac{V_{out}}{V_{in}} = \frac{\pi\left(\left(\frac{OD}{2}\right)^2 - R_{x=0}^2\right)}{\pi\left(R_{x=0}^2 - \left(\frac{ID}{2}\right)^2\right)} = 1.12 \quad (13)$$

Therefore, lines B and D are placed such that V_B and V_D are both equal to 1.12*V_A.

7.3.4 Correlate Measurement to an Upset

With $t_{FT,k}$ measured and the volume of flash calculated, the value of the increment of upset k must be determined. To make the correlation between flash thickness and upset, a conservation of volume is assumed so that the volume of the flash is equal to the volume displaced due to an upset.

The conservation of volume can be shown as:

$$V_{A,k} + V_{B,k} + V_{C,k} + V_{D,k} = U_k * \frac{\pi}{4}(OD^2 - ID^2) \quad (14)$$

Where U is upset. The left hand of the equation is the total volume in the flash as calculated previously and the right hand is the displaced volume calculated by multiplying upset by cross sectional area. By solving for upset in this equation, the average of the flash thicknesses can be correlated to the weld upset when lines A-D were extruded.

7.3.5 Evolution of λ Throughout Quasi-Steady State Stage

By placing line A at several different locations and following the above method for each location, a relationship between flash thickness and upset can be calculated. The results of repeating this process over one hundred times per weld are shown Figure 7-2. A linear relationship is fit to the data during the quasi-steady state stages of the welds (upset >1mm), as shown in Figure 7-2. The equation for the fit of the data to calculate λ is given as:

$$\lambda = 3.0205 * U - 3.4917 * F + 31.195 \quad (15)$$

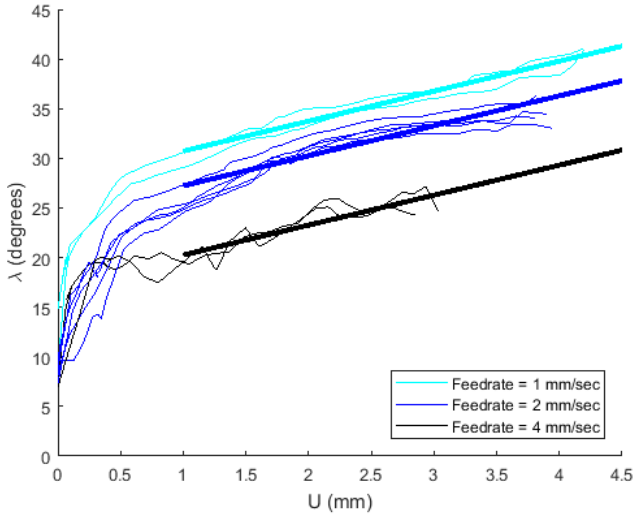

Figure 7-2. λ for all welds.

λ increases linearly during the quasi steady state stage of the weld process. The rate of increase is independent of feedrate. The magnitude of flash thickness for a given upset is linearly dependent upon feedrate, with faster feedrates resulting in thinner flashes.

7.4 Estimation of PSZ Thickness (t_{PSZ})

The thickness of the PSZ (t_{PSZ}) is necessary in the calculation of the three strain rates. In the proposed model, it is assumed that t_{PSZ} is uniform for all X at any given increment of upset, as shown in Figure 6-1. A uniform PSZ width is proposed to account for the fact that position variable P in Figure 3-3 had no statistically significant effect on the tracer radius, as shown by the results of the statistical study in section 3.5.2.

7.4.1 Calculation of t_{PSZ} at the End of a Weld

t_{PSZ} at the end of the weld can be calculated from the relationship fit of the tracer radii in Figure 3-4 using the following equation:

$$t_{PSZ,end} = \sqrt{2} * r_{tracer} \quad (16)$$

This equation is derived from the assumption that the material deformation within the PSZ is the quadrant of a circle, as shown in Figure 6-1. This equation is calculated for each of the three measurements of tracer radii.

7.4.2 Estimation of t_{PSZ} for Each Increment of Upset

t_{PSZ} during the weld process is unknown, but necessary to calculate strain rate throughout the weld process. To calculate t_{PSZ} during the process, previous studies in orthogonal assumed that the ratio between t_{PSZ} and l_{PSZ} to be constant [27]. Both t_{PSZ} and l_{PSZ} are depicted in Figure 6-1. Equations to predict the shear angle, and therefore l_{PSZ} have been previously defined and validated in orthogonal machining [28]. With a single measurement of the ratio between t_{PSZ} and l_{PSZ} along with an equation for l_{PSZ} during the process, studies in orthogonal machining can estimate the t_{PSZ} during the process.

l_{PSZ} can be calculated in tubular specimens at any increment of upset k using the following formula:

$$l_{PSZ,k} = \frac{OD-ID}{4cos(\lambda_k)} \quad (17)$$

With $l_{PSZ,k}$ calculated, t_{PSZ} can be estimated using the ratio similar to the method used in orthogonal machining. This estimation for a given increment of upset is defined as:

$$t_{PSZ,k} = l_{PSZ,k} * \frac{t_{PSZ}}{l_{PSZ}} \quad (18)$$

Where t_{PSZ}/l_{PSZ} is the ratio between the measurements. In orthogonal machining, this ratio is assumed constant. In the present study, this ratio is found as a function of λ.

7.4.3 Analysis of Ratio to Be Used in t_{PSZ} Estimate

The ratio between t_{PSZ} and l_{PSZ} is calculated at the end of the weld using the results of the μCT radii and shown in Figure 7-3 as a function of λ. A constant ratio would signify that there is no dependency upon any variables, including the angle of the PSZ (λ), as indicated by the horizontal dashed lines in Figure 7-3. The fit of the data, shown in Figure 7-3, shows that in RFW of thin wall tubes, the assumption of a constant ratio of PSZ length to thickness is not valid. The linear fit is used in the calculation of strain throughout the weld process.

7.4.4 t_{PSZ} Throughout Weld Process

Using the fit of the ratio t_{PSZ}/l_{PSZ} (Figure 7-3), λ (Figure 7-2), and the t_{PSZ} measurements at the end of the weld, t_{PSZ} is estimated throughout the weld process using Equation 18. This estimation is shown in Figure 7-4, which depicts how feedrate, upset, and tracer type affect t_{PSZ}.

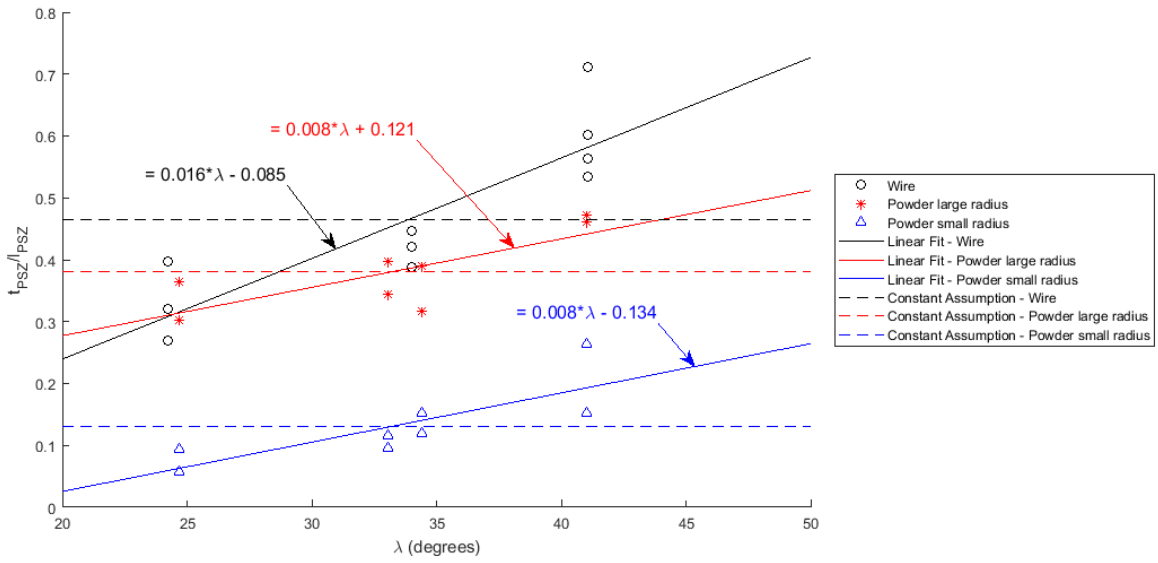

Figure 7-3. PSZ ratio using as a function of λ.

The crossing of the wire and powder large radii lines in F=4 mm/s is due to the extrapolation of the ratio depicted Figure 7-3. λ at the beginning of this weld is significantly less than 25 degrees.

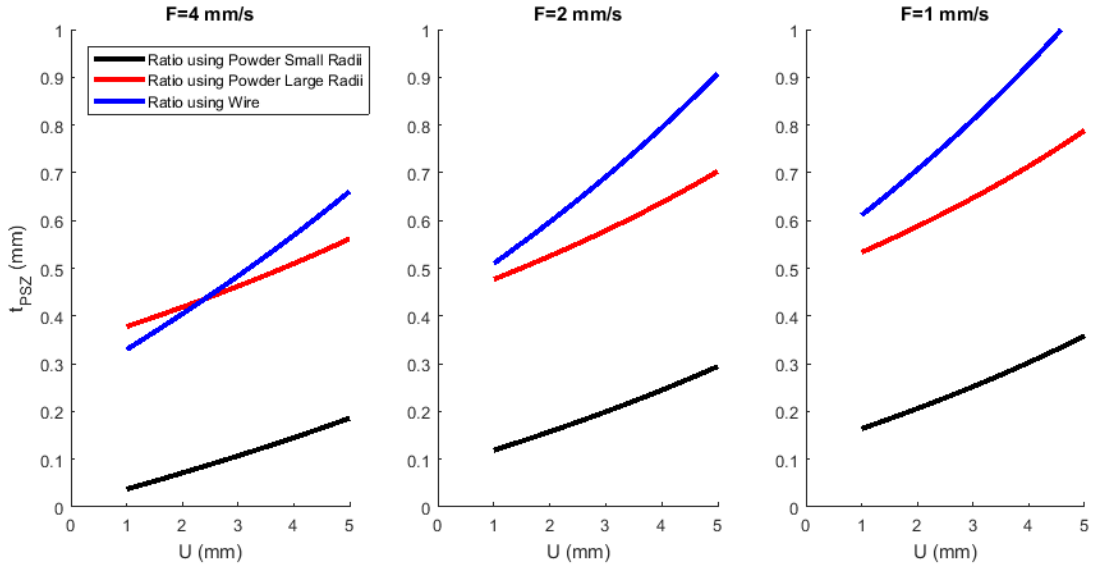

Figure 7-4. PSZ thickness throughout the weld process for all feedrates.

8 PSZ STRAIN AND STRAIN RATE

With the independent variables (F, ϕ, λ, and t_{PSZ}) available as continuous functions throughout the weld process, the strain and strain rate can be calculated using Equations 6, 7, 8, and 10.

8.1 Results of Strain and Strain Rate in the PSZ throughout the Weld Process

Figure 8-1 and Figure 8-2 show the evolution of the equivalent strain and mean equivalent strain, respectively, throughout the weld process. In Figure 8-2, the upper bounds, solid, come from using the data from the wire tracers and the lower bounds, dashed, come from using the data from the powder small radii, as shown in Figure 3-4 and Figure 7-4.

The magnitude of strain in Figure 8-1 is similar to the strain reported by studies of orthogonal machining and ECAP [21] [23]. This is expected since all processes undergo a similar deformation and use the same equation for calculating strain. For the current weld parameters, the true equivalent strain in the PSZ is between 1.2 and 1.8.

The strain far from the weld interface during the initial stage of RFW is expected to be much greater than the strain in the PSZ during the quasi-steady state stage. The flash thickness, and therefore λ, is much smaller in the initial stage, as shown in Figure 7-2. These values for λ can be used to estimate the strain during the initial stage, as is depicted as the thin lines in Figure 8-1. The material deformation is not investigated for this study. Therefore, the strain depicted in

Figure 8-1 is an extrapolation using the present analysis and should not be taken as the exact values of strain during the initial stage of RFW.

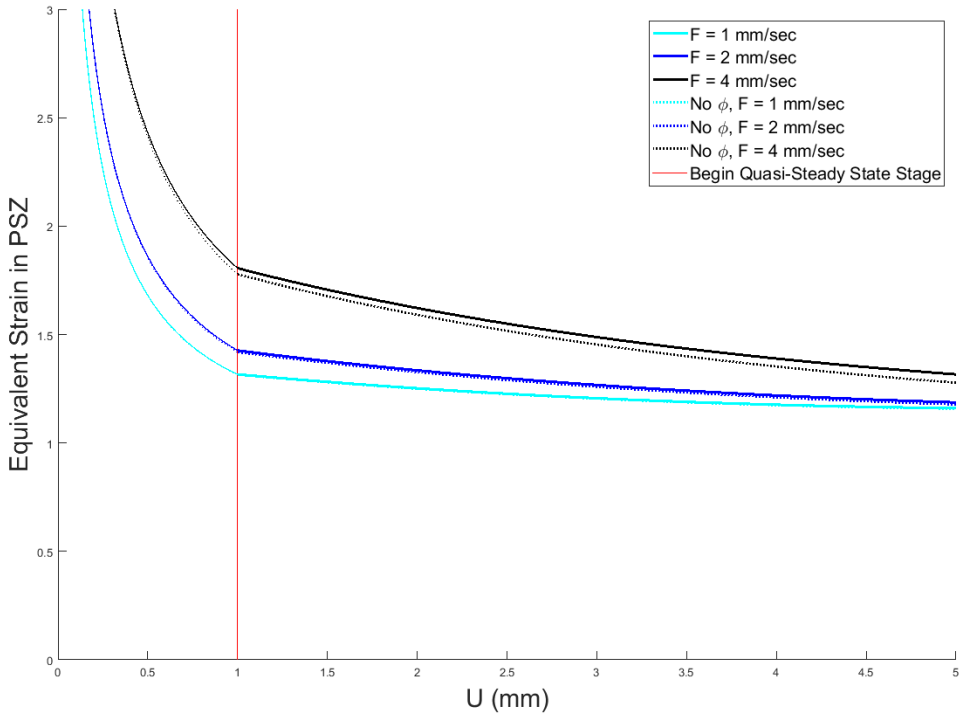

Figure 8-1. Equivalent strain throughout the weld process.

The mean true equivalent strain rate in the PSZ is between 10^0 and $10^{2.2}$. Unlike the values of λ, there is no current estimation of t_{PSZ} during the initial stage of RFW. Therefore, no estimation of the mean equivalent strain rate can be made. The strain rate is expected to be much higher than the values reported in Figure 8-2.

The range in mean strain rates shown in Figure 8-2 is much larger than the range of strains shown in Figure 8-1. This is due to the compounding effect feedrate has on decreasing both λ and PSZ thickness. Faster welds have larger values of strain and the distance over which the deformation occurs is smaller.

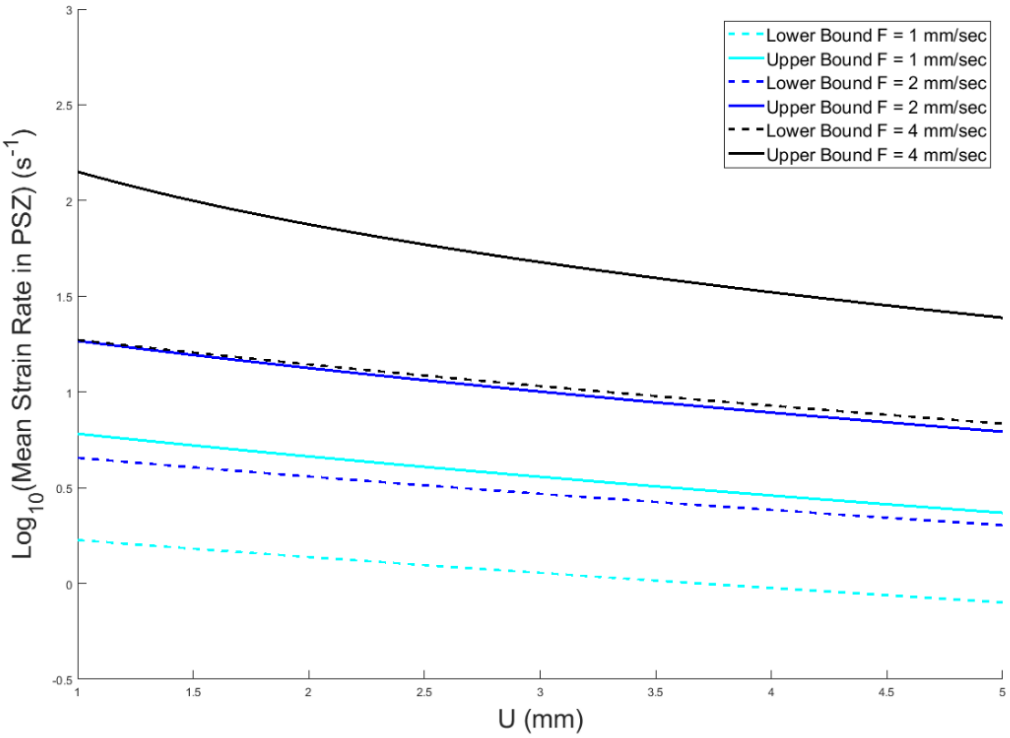

Figure 8-2. Mean equivalent strain rate throughout the weld process.

8.2 Comparison to Previous Studies

Strain rates in the PSZ, shown in Figure 8-2, are higher than that reported in previous RFW studies, as depicted in Figure 6-2. Midling reports strain rates around 10^0 [5], which is the lowest value for mean equivalent strain rate reported in the present model (Figure 8-1).

The strain rates reported in ECAP are around 3.8 [26] [29]. This is similar to the strain rate in the PSZ for feedrates between 1 and 2 mm/s. The strain rate in orthogonal machining is much higher than the strain rates reported in Figure 8-2 [23]. The higher strain rates in orthogonal machining are the result of the velocity of machining tools being much faster than 4 mm/s.

8.3 Assessment of Assumption of No Azimuthal Flow

Figure 8-1 also shows the error of the assumption of no azimuthal flow in Path 2 on the equivalent strain rate. The dashed line was calculated by removing $\gamma_{R\theta}$ and $\dot{\gamma}_{R\theta}$ in the calculation of equivalent strain (Equation 9) and equivalent strain rate, respectively. This calculation indicates the equivalent strain and strain rate with the assumption of no azimuthal flow. The assumption results in an error of 3% in the equivalent true strain and <1% in the mean equivalent true strain rate. The error in the strain rate is so small that it cannot be depicted in Figure 8-2.

8.4 Future Work

The application of this model to different materials and geometries does not require significant amount of work. With the assumption of no azimuthal flow, the only independent variables needed in future studies are λ and t_{PSZ}. Therefore, future studies will only have to calculate a new fit similar to Figure 7-2 and Figure 7-4. With the use of hardness maps and metallography, both of these fits can be calculated not using a μCT.

8.5 Limitations on Results of Strain and Strain Rate

The values for strain and strain rate reported in the current paper are not to be used as absolute bounds of what can be accomplished in RFW of thin walled tubes, but instead be viewed as ranges for typical values in normal operating parameters. Higher or lower strain rates could be accomplished with faster or slower feedrates than those used in the current experiment.

9 CONCLUSIONS

The present study provides new 3D insights on the material flow of RFW through the tungsten tracers. A new material flow model has been proposed that incorporates the insights found in the tracer study.

Similar to the model proposed by Midling et al. [5], the current model consists of two main deformation zones. The material far from the weld interface undergoes primarily radial flow (Path 2), while the material close to the weld interface undergoes primarily azimuthal flow (Path 1), as shown in Figure 4-1. Approximately 80% of the wall thickness flow through Path 2. The deformation characteristics in these zones are disparate, so separate analyses on the strain and strain rate are required.

The main difference in the present model and previous models is how the material in Path 2 transitions from axial flow to radial flow. The present analysis models this transition as an abrupt change, similar to orthogonal machining or ECAP, as depicted in Figure 6-1. This comparison is useful since the equations for strain and strain rate in both orthogonal machining and ECAP have been defined and validated.

The present study provides an experimentally validated analytical material flow model in RFW of tubes against which future FEA and other studies can be compared. By understanding the deformation during the weld process, better predictions of weld upset and forces are possible.

The material flow in the present study has been analyzed and quantified. The deformation in the model can be summarized as:

- The HGZ width in nickel-based superalloy 718 is between 0.15 and 0.2 mm.
- The material in the HGZ flows primarily in the azimuthal direction and exhibits strain rates between $10^{3.5}$ and $10^{3.7}$. The strain at temperature is sufficiently large for dynamic recrystallization.
- The material in the PSZ undergoes little azimuthal flow. The strain in this zone is between 1.2 and 1.8. The mean strain rate in the PSZ is between 10^{0} and $10^{2.2}$ s^{-1}.
- Both strain and strain rate decrease in the PSZ throughout the quasi-steady state stage of RFW.

REFERENCES

[1] M. Maalekian, "Friction welding - critical assessment of literature," *Science and Technology of Welding and Joining,* vol. 12, no. 8, pp. 738-759, 2007.

[2] P. Li, J. Li, X. Li, J. Xiong, F. Zhang and L. Liang, "A study of the mechanisms involved in initial friction process of continuous drive friction welding," *Journal of Adhesion Science and Technology,* p. 12461257, 2015.

[3] G. Bendzsak, T. Norht and Z. Li, "Numerical model for steady-state flow in friction welding," *Acta Materialia,* vol. 45, no. 4, pp. 1735-1745, April 1997.

[4] W. H. Beyer, CRC Standard Mathematical Tables, 28th ed., Boca Raton, FL: CRC Press, 1987.

[5] O. Midling and O. Grong, "A process model for friction welding of Al-Mg-Si and Al-SiC metal matrix compoxites - I. HAZ temperature and strain rate distribution," *Acta Metallurgica et Materialia,* vol. 42, no. 5, pp. 1595-1609, 1994.

[6] L. Fu, L. Duan and S. Du, "Numerical Simulation of Inertia Friction Welding Process by Finite Element Method," *Welding Journal,* vol. 82, pp. 65-70, 2003.

[7] B. Grant, M. Preuss, P. Withers, G. Baxter and M. Rowlson, "Finite element process modelling of inertia friction welding advanced nickel-based superalloy," *Materials Science and Engineering A,* vol. 513, pp. 366-375, 2009.

[8] A. Malakizadi, S. Cedergren, I. Sadik and L. Nyborg, "Inverse identification of flow stress in metal cutting process using Response Surface Methodology," *Simulation Modelling Practice and Theory,* vol. 60, pp. 40-53, 2016.

[9] L. Wang, M. Preuss, P. Withers, G. Baxter and P. Wilson, "Energy-Input-Based Finite-Element Process Modeling of Inertia Welding," *Metallurgical and Materials Transactions B,* vol. 36, no. 4, pp. 513-523, 2005.

[10] Q. Zhang, L. Zhang, W. Liu, X. Zhang, W. Zhu and S. Qu, "3D rigid viscoplastic FE modelling of continuous drive friction welding process," *Science and Technology of Welding and Joining,* vol. 11, no. 6, pp. 737-743, 2006.

[11] L. D'Alvise, E. Massoni and S. Walloe, "Finite element modelling of the inertia friction welding process between dissimilar materials," *Journal of Materials Processing Technology,* vol. 125, pp. 387-391, 2002.

[12] P. Li, J. Li and H. Dong, "Analytical description of heat generation and temperature field during the inititial stage of rotary friction welding," *Journal of Manufacturing Processes,* vol. 25, pp. 181-184, 2017.

[13] J. Healy, D. Mcmullan and A. Bahrani, "Analysis of frictional phenomena in friction welding of mild steel," *Wear,* vol. 37, no. 2, pp. 265-278, 1976.

[14] Y. Kim, A. Fuji and T. North, "Residual stress and plastic strain in AISI 304L stainless steel/titanium friction welds," *Material Science and Technology,* vol. 11, no. 4, pp. 383-388, 1995.

[15] A. Francis and R. Craine, "On a model for frictioning stage in friction welding of thin tubes," *International Journal of Heat Mass Transfer,* vol. 28, no. 9, pp. 1747-1755, 1985.

[16] W. Li and F. Wang, "Modeling of continuous drive friction welding of mild steel," *Materials Science and Engineering A,* vol. 528, pp. 5921-5926, 2011.

[17] J. Xiong, J. Li, Y. Wei, F. Zhang and W. Huang, "An analytical model of steady-state continuous drive friction welding," *Acta Materialia,* vol. 61, pp. 1662-1675, 2013.

[18] M. Kessler, S. Suenger, M. Haubold and M. Zaeh, "Modeling of upset and torsional moment during inertia friction welding," *Journal of Materials Processing Technology,* vol. 227, pp. 34-40, 2016.

[19] J. Akram, P. R. Kalvala, V. Jindal and M. Misra, "Evaluating location specific strain rates, temperatures, and accumulated strains in friction welds through microstructure modeling," *Defence Technology,* pp. 1-10, 2017.

[20] P. Sketchley, P. Threadgill and I. Wright, "Rotary friction welding of an Fe3Al based ODS alloy," *Materials Science and Engineering,* vol. 329, pp. 756-762, 2002.

[21] D. Lee, "An upper-bound solution of channel angular deformation," *Scripta Materialia,* vol. 43, no. 2, pp. 115-118, 2000.

[22] Y. Iwahashi, J. Wang, Z. Horita, M. Nemoto and T. Langdon, "Principle of equal-channel angular pressing for the processing of ultra-fine grained materials," *Scripta Materialia,* vol. 35, pp. 143-146, 1996.

[23] H. Kishawy and L. Pang, "A phenomenological modeling of deformation during methal cutting: a modified thick shear zone analysis," *Journal of Engineering Manufacture,* vol. 226, no. 9, pp. 1431-1441, 2012.

[24] J. Davim and C. Maranhao, "A study of plastic strain and plastic strain rate in mahcining of steel AISI 1045 using FEM analysis," *Materials and Design,* vol. 30, pp. 160-165, 2009.

[25] D. Lalwani, N. Mehta and P. Jain, "Extension of Oxley's predictive machining theory for Johnson and Cook flow stress model," *Journal of Materials Processing Technology,* vol. 209, pp. 5305-5312, 2009.

[26] R. Z. Valiev and T. G. Langdon, "Principles of equal-channel angular pressing as a processing tool for grain refinement," *Progress in Materials Science,* vol. 51, pp. 881-981, 2006.

[27] P. Oxley, The mechanics of machining: an analytical approach to assessing machinability, New York: Ellis Horwood, 1989.

[28] E. M. Merchant, "Mechanics of the Metal Cutting Process. I. Orthogonal Cutting and a Type 2 Chip," *Journal of Applied Physics,* vol. 16, no. 5, pp. 267-275, 1945.

[29] S. Semiatin, D. Delo and E. Shell, "The effect of material properties and tooling design on deformation and fracture during equal channel angular extrusion," *Acta Materialia,* vol. 48, pp. 1841-1851, 2000.

[30] P. Kelly, Solid mechanics part I: An introduction to solid mechanics, Auckland, New Zealand: University of Auckland, 2013.

10 APPENDIX A. DERIVATION OF $\gamma_{x\theta}$ AND $\gamma_{y\theta}$

This appendix demonstrates how the shear strain caused by azimuthal flow in the PSZ is rotated from the RZθ coordinate frame into the XYθ coordinate frame. The coordinate frames and the model of the PSZ in the RZ plane are shown in Figure A-1.

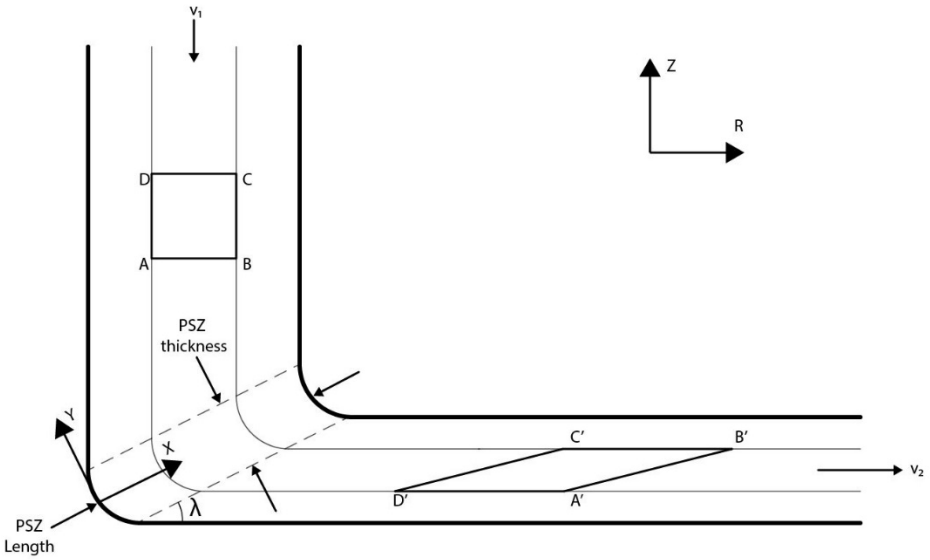

Figure A-1. Model of the PSZ in the RZ plane.

Azimuthal flow cannot be depicted in Figure A-1. The azimuthal flow of Path 2 is depicted in Figure A-2.

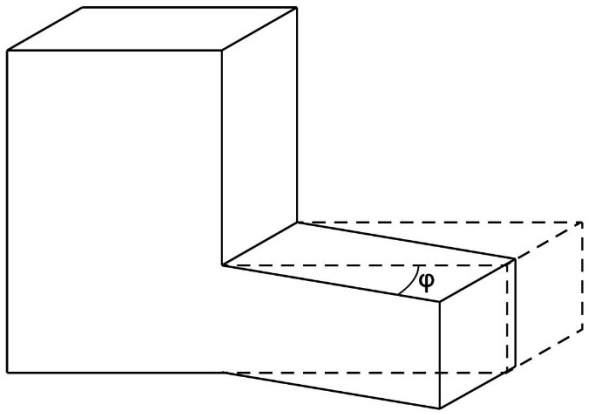

Figure A-2. 3D flow of Path 2.

The strain due to the azimuthal flow is defined as:

$$\gamma_{R\theta} = \tan(\Phi) \tag{19}$$

This strain is in the RZθ coordinate system, while the shear strain from Equation 6 is in the XYθ coordinate system. This rotation is performed using a transformation matrix described as [30]:

$$[Q] = \begin{bmatrix} \cos(x_1, x_1') & \cos(x_1, x_2') & \cos(x_1, x_3') \\ \cos(x_2, x_1') & \cos(x_2, x_2') & \cos(x_2, x_3') \\ \cos(x_3, x_1') & \cos(x_3, x_2') & \cos(x_3, x_3') \end{bmatrix} \tag{20}$$

Where $\cos(x_i, x_j')$ is measured between the base coordinate system and the rotated coordinate system. The rotation is performed by the following equation [30]:

$$[\varepsilon'] = [Q'][\varepsilon][Q] \tag{21}$$

Where the strain matrix is defined as [30]:

$$[\varepsilon] = \begin{bmatrix} \varepsilon_{11} & \varepsilon_{12} & \varepsilon_{13} \\ \varepsilon_{21} & \varepsilon_{22} & \varepsilon_{23} \\ \varepsilon_{31} & \varepsilon_{32} & \varepsilon_{33} \end{bmatrix} \tag{22}$$

By applying these equations to the coordinate systems used in the present paper, the following equation depicts the transformation matrix Q for rotation of value λ about the θ axis in order to transform from the RZθ frame to the XYθ frame:

$$[\mathrm{Q}] = \begin{bmatrix} \cos(\mathrm{R},\mathrm{X}) & \cos(\mathrm{R},\mathrm{Y}) & \cos(\mathrm{R},\theta) \\ \cos(\mathrm{Z},\mathrm{X}) & \cos(\mathrm{Z},\mathrm{Y}) & \cos(\mathrm{Z},\theta) \\ \cos(\theta,\mathrm{X}) & \cos(\theta,\mathrm{Y}) & \cos(\theta,\theta) \end{bmatrix} \tag{23}$$

$$= \begin{bmatrix} \cos(\lambda) & \cos(\lambda+90°) & 0 \\ -\cos(\lambda+90°) & \cos(\lambda) & 0 \\ 0 & 0 & 1 \end{bmatrix} \tag{24}$$

The strain matrix for the azimuthal strain in the RZθ frame is defined as:

$$[\varepsilon] = \begin{bmatrix} \varepsilon_{\mathrm{RR}} & \varepsilon_{\mathrm{RZ}} & \varepsilon_{\mathrm{R}\theta} \\ \varepsilon_{\mathrm{ZR}} & \varepsilon_{\mathrm{ZZ}} & \varepsilon_{\mathrm{Z}\theta} \\ \varepsilon_{\theta\mathrm{R}} & \varepsilon_{\theta\mathrm{Z}} & \varepsilon_{\theta\theta} \end{bmatrix} \tag{25}$$

$$= \begin{bmatrix} 0 & 0 & \tan(\phi) \\ 0 & 0 & 0 \\ -\tan(\phi) & 0 & 0 \end{bmatrix} \tag{26}$$

Combining Equations 6, 19, 23, and 23 results in the rotated shear strain caused by the azimuthal flow to be defined as:

$$[\varepsilon'] = \begin{bmatrix} \varepsilon_{\mathrm{XX}} & \varepsilon_{\mathrm{XY}} & \varepsilon_{\mathrm{X}\theta} \\ \varepsilon_{\mathrm{YX}} & \varepsilon_{\mathrm{YY}} & \varepsilon_{\mathrm{Y}\theta} \\ \varepsilon_{\theta\mathrm{X}} & \varepsilon_{\theta\mathrm{Y}} & \varepsilon_{\theta\theta} \end{bmatrix} \tag{27}$$

$$= \begin{bmatrix} 0 & 0 & \cos(\lambda)\tan(\phi) \\ 0 & 0 & -\cos(\lambda+90°)\tan(\phi) \\ -\cos(\lambda)\tan(\phi) & \cos(\lambda+90°)\tan(\phi) & 0 \end{bmatrix} \tag{28}$$

The individual components of $[\varepsilon']$ can be defined as:

$$\gamma_{\mathrm{X}\theta} = \tan(\Phi) * \cos(\lambda) \tag{29}$$

$$\gamma_{Y\theta} = -\tan(\Phi) * \cos(\lambda+90°) \tag{30}$$

11 APPENDIX B. TABLE OF TRACER DATA

Table B-1. Table of all tracer data

Tracer Type	Feedrate (F)	Position (P)	ϕ	Wire Radius	Powder Small Radius	Powder Large Radius	λ_{end}
Wire	4	0.1422	21.2226	0.3972	NA	NA	24.2527
Wire	4	0.2071	35.3008	0.3198	NA	NA	24.2527
Wire	4	0.0113	87.7112	NA	NA	NA	24.2527
Wire	4	-0.2990	23.8515	0.2686	NA	NA	24.2527
Wire	2	-0.2169	12.0884	0.4847	NA	NA	34.0073
Wire	2	0.1964	12.1726	0.4568	NA	NA	34.0073
Wire	2	-0.2972	15.0738	0.4217	NA	NA	34.0073
Wire	2	-0.0189	86.2177	NA	NA	NA	34.0073
Wire	1	-0.1880	7.4540	0.7160	NA	NA	41.0523
Wire	1	0.2129	8.5301	0.8473	NA	NA	41.0523
Wire	1	-0.2989	10.2334	0.6708	NA	NA	41.0523
Wire	1	0.0079	6.0739	0.6370	NA	NA	41.0523
Powder	2	-0.1944	17.1457	NA	0.1250	0.4274	33.0407
Powder	2	0.2136	6.7182	NA	0.1023	0.3712	33.0407
Powder	2	-0.2346	15.7808	NA	0.1667	0.4250	34.4165
Powder	2	0.0686	76.4274	NA	0.1312	0.3469	34.4165
Powder	2	-0.0763	84.4940	NA	NA	NA	35.6232
Powder	2	-0.0202	82.9646	NA	NA	NA	36.2598
Powder	1	-0.1783	8.5259	NA	0.1805	0.5629	41.0201
Powder	1	0.2190	7.5639	NA	0.3137	0.5500	41.0201
Powder	4	0.1952	34.0947	NA	0.0957	0.3043	24.6913
Powder	4	0.2144	31.7886	NA	0.0582	0.3672	24.6913